Assembly of Aggregation-Induced Emission Active Bola-Amphiphilic Macromolecules into Luminescent Nanoparticles Optimized for

pubs.acs.org/Biomac

Article

Assembly of Aggregation-Induced Emission Active Bola-Amphiphilic Macromolecules into Luminescent Nanoparticles Optimized for Two-Photon Microscopy In Vivo

Jean Rouillon, Lamiaa M. A. Ali, Kamel Hadj-Kaddour, Raphaël Marie-Luce, Guillaume Simon, Mélanie Onofre, Sandrine Denis-Quanquin, Marion Jean, Muriel Albalat, Nicolas Vanthuyne, Guillaume Micouin, Akos Banyasz, Magali Gary-Bobo,* Cyrille Monnereau,* and Chantal Andraud

Cite This: *Biomacromolecules* 2022, 23, 2485−2495

Read Online

ACCESS | Metrics & More | Article Recommendations | Supporting Information

ABSTRACT: The (Z) and (E)-isomers of an extended tetraphenylethylene-based chromophore with optimized two-photon-induced luminescence properties are separated and functionalized with water-solubilizing pendant polymer groups, promoting their self-assembly in physiological media in the form of small, colloidal stable organic nanoparticles. The two resulting fluorescent suspensions are then evaluated as potential two-photon luminescent contrast agents for intravital epifluorescence and two-photon fluorescence microscopy. Comparisons with previously reported works involving similar fluorophores devoid of polymer side chains illustrate the benefits of later functionalization regarding the control of the self-assembly of the nano-objects and ultimately their biocompatibility toward the imaged organism.

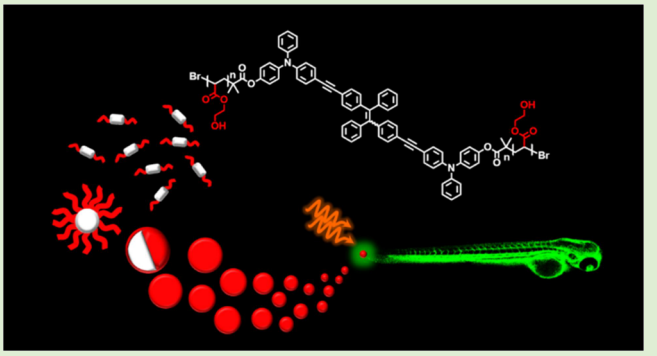

INTRODUCTION

Since its invention in the late 1990s, two-photon fluorescence microscopy has experienced impressive developments[1,2] and has opened unprecedented perspectives in tissue imaging that have substantially benefited such diverse fields as neurobiology,[3] physiology,[4] embryology,[5] and tissue engineering.[6] These developments have been achieved thanks to combined advances in the optical design setup and in the developments of increasingly sophisticated and selective endogenous (green fluorescent proteins)[7] and exogenous (synthetic organic chromophores and nanoparticles) fluorescent contrast agents.[8−11] In this framework, the conception of molecular probes or nano-objects that combine sizeable two-photon-induced emission properties with good solubility (or colloidal stability) in physiological media has been a major issue, on which we have been extensively working in recent years.[12−14]

In previous reports, we have proposed chromophore functionalization with water solubilizing poly(hydroxyethylacrylate) (PHEA) polymeric side chains as a relevant approach to achieve high biocompatibility of molecular bioprobes.[15] We have shown that this functionalization could efficiently shield the molecule from interactions with its local environment, ensuring the solubility of inherently lipophilic and prone-to-stacking fluorophores into aqueous media and keeping luminescence efficiencies high. This strategy has been used in the making of fluorophores that have already found promising application in diverse biorelated applications such as intravital imaging of cerebral vascularization[16−18] or the detection of biomolecules (ds-DNA,[19] G-quadruplexes,[20,21] and proteins[22]) in complex physiological media. In parallel, we have recently reported on extended tetraphenylethylene (TPE) derivatives—a class of molecules classically used for their aggregation-induced emission (AIE) properties,[23−25] in particular for bioimaging and biosensing applications[26−31]—that had been specifically designed to maximize the two-photon emission properties of their aggregates.[32] During this study, it turned out that, despite the excellent colloidal stability and excellent spectroscopic properties of the suspension obtained by the nanoprecipitation of $\mathbf{TT}^{\mathbf{OMe}}$, only limited control over the assembly was achieved: as a result, mixtures of large (d > 100 nm) and disperse nanoparticles were obtained with detrimental outcome on the long-term survival of the imaged zebrafish.

It has already been established in previous literature reports that the self-assembly of fluorophores containing macro-

Received: February 21, 2022
Revised: May 11, 2022
Published: May 24, 2022

https://doi.org/10.1021/acs.biomac.2c00232
Biomacromolecules 2022, 23, 2485−2495

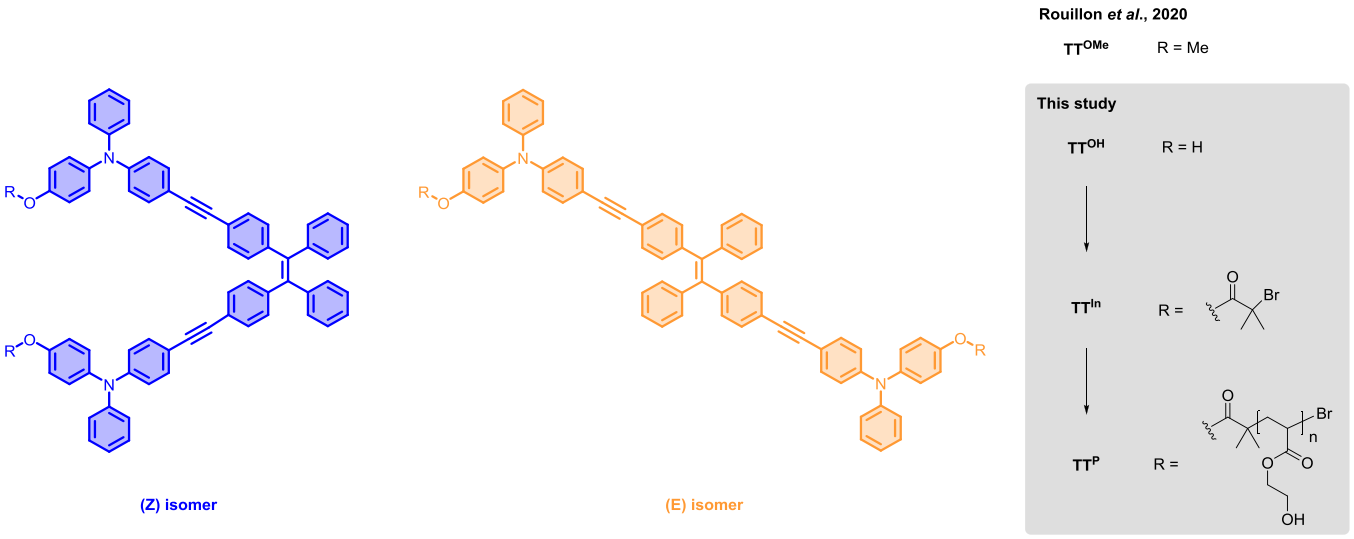

Figure 1. Chemical structure of **(E/Z)TT^{P}** and its precursors.

molecules (either in the form of grafted polymers or conjugated polymers) usually led to smaller and better controlled self-assembly compared to the dye-loaded nano-objects obtained by conventional nanoprecipitation methods.[33] In particular, direct self-assembly of fluorescent amphiphilic polymers upon dispersion in aqueous media has proved to be a remarkably effective approach for the synthesis of small (10–14 nm) monodisperse nanoparticles, well suited for in vivo applications,[34] while larger nanoparticles (>100 nm, typically) are rapidly cleared from the bloodstream upon internalization within macrophages and tend to induce more severe adverse effects such as acute inflammations.[35]

In this work, aiming to further explore such extended TPE derivatives and taking advantage of our abovementioned longtime expertise in the functionalization of lipophilic fluorophores through controlled radical polymerization, we have synthesized and studied **TT^{P}**, a new two-photon-absorbing, water-soluble, and AIE-active luminescent probe, that can be derived into two stereoisomers differing by the stereoconfiguration of their central double bond (Figure 1). Through a combined study, involving DLS and DOSY NMR, we investigate the self-assembly process of both isomers and their mixture in aqueous suspensions. In particular, we show that, owing to the amphiphilic macromolecular nature of the molecule, it is possible to obtain controlled small-sized (ca. 10 nm) nanoassemblies of the chromophores under either their (Z) or (E)-forms in both pure water and physiological media. The resulting colloidal suspensions combine the significant two-photon absorption (2PA) cross sections and AIE efficiencies, making them suitable for two-photon fluorescence microscopy in living biological systems. Comparison of our previously studied assemblies of pure nanoprecipitated **(E/Z)TT^{OMe}** chromophores[32] on several days after injection into zebrafish embryos clearly demonstrates the benefits of polymer functionalization and underlines the biocompatibility of these resulting nano-objects.

MATERIALS AND METHODS

Synthesis. Syntheses were performed in oven-dried vessels purged with argon. Solvents were dried on 3 Å molecular sieves. The reactions were monitored by analytical thin layer chromatography (TLC) on a Merck 60 F-254 precoated silica gel plate (0.2 mm thickness), and the products were revealed by a UV lamp. Purification by column chromatography was made over Merck silica gel 60 (0.040–0.063 mm).

All newly synthesized compounds were routinely characterized by ^{1}H and ^{13}C NMR and high-resolution mass spectrometry (HRMS). Detailed synthetic protocols and characterization data, including NMR spectra, are available as Supporting Information (S1 and S2, Figures S2–S15).

NMR Studies. NMR spectra were recorded on a Bruker Avance III 400 MHz spectrometer equipped with a Prodigy Cryoprobe. The temperature was regulated at 298 K. Chemical shifts are reported as values (ppm) with reference to the solvent residual peak of $CDCl_3$, DMSO-d_6, or D_2O. Abbreviations for the ^{1}H NMR data: chemical shift, δ; multiplicity (s = singlet, d = doublet, t = triplet, q = quartet, and m = multiplet); coupling constants, J.

For diffusion experiments, a bipolar pulse longitudinal eddy current delay (BPPLED) pulse sequence was chosen, and the diffusion time was set to 250 ms. Sine-shaped pulse field gradient was used with a length of 2.5 ms, and the gradient intensity was linearly incremented from 0.963 to 47.187 G cm^{-1} over 30 experiments. After each gradient pulse, 200 ms delay was used as a recovery delay.

DOSY NMR was generally processed by Mestrelab MNova using Bayesian transformation. Polydispersity of the polymer was determined thanks to the maximum entropy methodology, processed on NMRNotebook.[36]

Dynamic light scattering (DLS) was recorded with a Malvern Instruments Zetasizer nano series instrument (with solutions at 10^{-5} M concentration).

HRMS measurements were performed at the *Centre Commun de Spectrométrie de Masse* (CCSM) of Lyon (France).

Preparative Separation of (E) and (Z)-Isomers. The separation of the (E) and (Z)-isomers was done on the compound **(E/Z)TT^{In}** using a chiral stationary phase, an amylose tris-(3,5-dimethylphenylcarbamate). Sixty successive injections on Chiralpak IA (250 × 10 mm), with hexane/2-PrOH/dichloromethane (90/5/5) as the mobile phase at 5 mL·min^{-1}, allowed to obtain 29 mg of the first eluted isomer, **(Z)TT^{In}**, and 38 mg of the second eluted isomer, **(E)TT^{In}** (chromatograms in Figure S16).

Surface Tension (SFT) Measurements. Six aqueous solutions of **(E/Z) TT^{P}** were prepared from the successive dilutions of 42.7 μmol/L solution of the polymer surfactant in ultrapure water (HPLC grade, Sigma-Aldrich). Prior to the SFT measurements, their density was measured with a DMA 5000 M densimeter from Anton Paar.

The surface tension of seven polymer surfactant solutions was measured by the pendant drop method, with a DSA 30E tensiometer, from Krüss, controlled by the supplier's software, Advance.

https://doi.org/10.1021/acs.biomac.2c00232
Biomacromolecules 2022, 23, 2485–2495

The pendant drop method is an optical way to obtain the SFT of a liquid in gas phase by solving the Young−Laplace equation:[37]

$$\Delta P = \Delta P_0 - \Delta\rho g z = \sigma\left(\frac{1}{R_1} + \frac{1}{R_2}\right)$$

where σ is the surface tension, R_1 and R_2 are the radii of curvature, g is the gravitational constant, z is the spatial coordinate, $\Delta\rho$ is the density difference between the liquid phase and the gas phase, ΔP is the pressure difference, and ΔP_0 is the reference pressure at $z = 0$. The Young−Laplace equation can be expressed in a cylindrical referential with three equations giving the coordinates, using the drop shape factor B:

$$B = \frac{\Delta\rho g R_0^2}{\sigma}$$

where R_0 is the radius of curvature at the apex of the drop. The computational Young−Laplace fit of the drop shape allows to calculate B and thus the surface tension σ.

For the SFT measurements of each concentration, a 500 μL glass Hamilton syringe was filled with the solution and vertically positioned in the tensiometer. The syringe plunger was slowly pushed by an automated program, in order to form progressively a drop at the tip of a stainless steel needle (ø = 1.826 mm). From the image taken with the camera of the system, the calibration made with the diameter of the needle, and the known densities of the air phase and the liquid, the software could analyze the drop shape and solve the Young−Laplace equation. The surface tension was measured at regular time intervals until the drop went out of the frame. Two or three drops were analyzed for each solution, and the stable data points were kept, so that it was possible to obtain a consistent average of surface tension, from a high number of data points (>100 points).

Spectroscopic Measurements. Absorption spectra (UV−vis) were recorded with a Jasco 670 spectrometer. Fluorescence spectra were recorded on a Horiba Jobin-Yvon Fluorolog-3 spectrofluorometer. The spectra were reference-corrected for both the excitation source light intensity variation (lamp and grating) and the emission spectral response (detector and grating). Emission spectra were recorded at 350 nm as the excitation wavelength. For the comparison of the emission spectra of the compound in various water/DMSO mixtures, spectra were normalized to their respective absorbance. Absolute fluorescence quantum yields were measured with a calibrated integrative sphere (2π steradians covered with spectralon, model G8 from GMP), as described in the literature.[1] Each sample was placed on a quartz tube at the concentration of 2×10^{-5} M. Four measurements were made with constant excitation and emission to give four integrated intensities. E_c and E_a are the integrated fluorescence spectra of direct excitation with and without the sample, respectively. L_c and L_a are the integrated excitation spectra of the sphere with and without the sample, respectively. A density filter (transmittance = 0.5%) was used to reduce the intensity of the excitation profile. Quantum yield is calculated according to the eq 1:

$$\Phi_{fluo} = \frac{E_c - E_a}{f(L_a - L_c)} \quad (1)$$

Two-Photon Absorption Cross-Section Measurements. Two-photon excitation spectra of the studied compounds were measured by the two-photon excitation-induced fluorescence technique in the 700−900 nm range. The excitation source was a tunable femtosecond Ti:sapphire laser (Chameleon Ultra I, Coherent). The laser beam was focused into a 10 × 10 cm quartz (QZS) cell using a 100 mm focal length lens. The cell containing the sample was positioned to minimize the optical path of the exciting laser and that of the emitted fluorescence in the sample, thus minimizing the inner filter effects and other artifacts. The emitted fluorescence was collected at 90° with respect to the excitation, filtered by adapted low-pass filters, and detected by a fiber-optic spectrometer (AvaSpec-EVO, Avantes).

The excitation power was measured by a thermal detector (S405C, Thorlabs). It was first verified that 2PA-induced fluorescence showed quadratic excitation power dependence at 720 nm for all compounds. Then, power was set to 40 mW for the measurement of the two-photon spectra. 2PA-induced fluorescence spectra did not show excitation wavelength dependence. Moreover, we checked in each case that the corrected fluorescence signal overlapped very well with the one-photon absorption (1PA)-induced fluorescence spectra.

The 2PA cross sections were calculated based on the integration of the fluorescence signals, by comparison with that of a fluorescein solution (10^{-5} mol·L^{-1}; pH = 13) as a 2PA standard, taken from the most recent literature.[38]

TEM Grid Preparation. A solution of 1 mg·mL^{-1} of the product was diluted (5 μL in two drops of water) in an Eppendorf tube and submitted to a quick sonication for 20 s. Then, 5 μL of solution in the Eppendorf tube was deposited as a droplet on the TEM grid. The obtained droplet was dried and removed from the grid with a thin cotton sheet. TEM observations were conducted on a JEOL 2100F-200 kV FEG system; HRTEM imaging was not made. The features of the TEM grid are as follows: lacey carbon film with a continuous layer of ultrathin carbon film (around 3 nm thickness), LC400-CU-CC25, by Electron Microscopy Sciences.

Cell Culture. Human breast cancer cells MCF-7 (purchased from ATCC) were cultured in DMEM/F-12 medium with GlutaMAX-I (containing 4.5 g·L^{-1} of D-glucose) supplemented with 10% fetal bovine serum and 1% penicillin/streptomycin. Cells were grown at 37 °C in humidified atmosphere with 5% CO_2.

Cytotoxicity Study. MCF-7 cells were seeded in a 96-well plate and incubated with increasing concentrations (from 2.5 to 150 μg·mL^{-1}) of the different **TT**^{P} isomers for 3 days, and the percentage of living cells was quantified by MTT assay. This consists in a colorimetric test performed using 3-(4,5-dimethylthiazol-2-yl)-2,5-diphenyltetrazolium bromide (Promega), where cells were incubated with 0.5 mg·mL^{-1} MTT for 4 h to determine the mitochondrial enzyme activity. Then, MTT precipitates were dissolved in 150 μL ethanol/DMSO solution (in 1/1 proportion), followed by 20 min of shaking, and absorbance was read at 540 nm. Cells treated with the vehicle served as control.

Imaging Potential In Vitro. The cellular uptake experiment was performed using confocal fluorescence microscopy on living cells. Cells were seeded (10^6 cells·cm^{-2}) on culture dishes with a glass bottom (Fluorodish from World Precision Instruments, Stevenage, UK). After seeding, cells were incubated with 50 μg·mL^{-1} of (E) or (Z)-isomers for 24 h. Cells were also loaded for 15 min with CellMask (Invitrogen, Cergy Pontoise, France) at 5 μg·mL^{-1} for membrane staining. Then, cells were washed twice with culture medium, and fluorescence imaging was performed on living cells with a *LSM780 LIVE* confocal microscope (*Carl Zeiss*, Le Pecq, France) at 750 nm for isomer detection and 561 nm for cell membranes. All images were obtained with a high magnification (Plan-Apochromat 40×/1.3 Oil DIC).

Zebrafish Breeding. Casper zebrafish embryos were purchased from Zebrafish International Resource Center (ZIRC) and raised to adulthood in a circulating aquarium system at 28 °C and 14 h light/10 h dark cycle, in the Molecular Mechanisms in Neurodegenerative Dementia (MMDN) laboratory (Inserm U1198), Montpellier University. Experiments with zebrafish embryos were performed according to the EU Directive 2010/63/EU on the protection of animals used for scientific purposes.

Imaging on Casper Zebrafish Embryos. Casper zebrafish embryos of 72 h post fertilization (hpf) were intravenously injected with 10 nL of (Z) or (E) **TT**^{P} isomers at 1 mg mL^{-1} concentration (n = 7 for control, n = 9 for (Z)-isomer, and n = 10 for (E)-isomer). One hour after injection, the embryos were observed using a one-photon excitation microscope at the excitation wavelength of 340−380 nm; then, the embryos were observed using a two-photon excitation confocal microscope at an excitation wavelength of 750 nm.

Toxicity Study on Zebrafish Embryos. After injections, embryos were maintained 3 days under breeding conditions, and everyday, the biocompatibility of the (Z)-isomer and (E) **TT**^{P} isomers

https://doi.org/10.1021/acs.biomac.2c00232
Biomacromolecules 2022, 23, 2485−2495

was analyzed according to various parameters relating the good development of embryos, such as mobility, heart rate, malformations, and death.

RESULTS AND DISCUSSION

Synthesis. All molecules discussed in the following are presented in Figure 1. Synthesis of the (E/Z)TT^{In} macroinitiator was adapted from the method previously published by us for the (E/Z)TT^{OMe} molecule,[32] keeping here the phenolic function free from the beginning (Scheme S1, detailed synthetic procedures available in the Supporting Informations, S1). Thus, Buchwald−Hartwig coupling between 4-hydroxydiphenylamine and para-bromo-iodobenzene was achieved with a good yield to afford 4-bromo-*N*-(4-hydroxyphenyl)-diphenylamine (**1**) thanks to a procedure compatible with free phenolic moieties.[39]

Then, a palladium-catalyzed Sonogashira cross-coupling with (triisopropylsilyl)acetylene yielded alkyne **2**, which was in turn deprotected with TBAF. The instable free alkyne as obtained was directly engaged in Sonogashira coupling with **TPE-Br** (Scheme S1) to lead to (E/Z)TT^{OH}. Finally, esterification between the (E/Z)TT^{OH} diol and 2-bromo-2-methylpropionyl led to the target macroinitiator (E/Z)TT^{In}. This synthesis being nonstereoselective, separation of the macroinitiator diastereoisomers was required to afford stereopure versions of the chromophore. It was herein performed on amylose-based chiral stationary phase (Figure S16), the efficiency of which has already been demonstrated by us on similar chromophores.[32]

The controlled polymerizations of (E/Z)TT^{In} as an (E/Z)-mixture, and also in stereopure form, were carried out in bulk 2-hydroxyethyl acrylate (HEA) monomer, using 2,2′-bipyridine and copper(I) bromide as a catalytic system, as already described in previous reports for the elaboration of related polymer−chromophore adducts.[15−18] The characteristic signatures of the aromatic part of the ^{1}H NMR spectra confirm that stereopurity has been preserved after the ATRP reaction and purification (Figure S13). Measurements of chain lengths and evaluation of polydispersity were achieved by ^{1}H NMR (Figure S14) and ^{1}H DOSY NMR (Figure S18), respectively, which will be discussed in the corresponding NMR study section. In all polymerization cases reported herein, a rigorous control of the polymerization kinetics makes it possible to obtain a range of target chain lengths in a controlled manner with low polydispersity (vide infra), which is essential for the comparison of the systems.

Spectroscopic Studies. Then, the spectral features of (E/Z)TT^{P} (n = 16) were studied in DMSO. The absorption and emission spectra are presented in Figure 2, while the main spectroscopic data are gathered in Table 1. First, we notice that the spectral signatures of (E/Z)TT^{P} (Figure 2) correspond well to those observed for their parent monomeric equivalent (E/Z)TT^{OMe}, which can be summarized as follows: (i) a structureless ICT band, typical of a large π-conjugated system; (ii) a large Stokes shift (ca. 6500 cm^{-1}) indicating significant reorganization processes between the ground and excited electronic states; (iii) an absorption band of the (Z)-isomer slightly blue-shifted (λ_{abs} = 357 nm) with respect to the (E)-isomer (λ_{abs} = 374 nm) and a reversed behavior for the emission with λ_{em} = 543 nm for the (Z)-isomer and 530 nm for the (E)-isomer of TT^{P}; and (iv) a similar two-photon absorption cross section σ_{2PA} for the (Z)-isomer as for the (E)-isomer (140 vs 100 GM) in the same range of wavelength

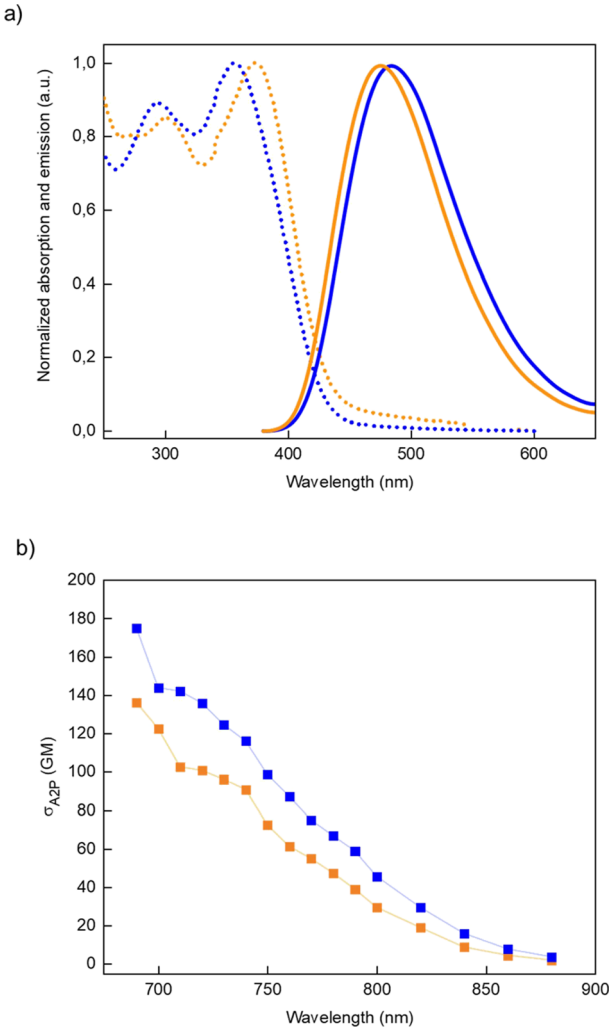

Figure 2. (a) Absorption (dashed) and emission (solid lines) spectra of the (E)-isomer (orange) and (Z)-isomer (blue) of TT^{P} in DMSO. (b) TPEF spectra of the (E)-isomer (orange) and (Z)-isomer (blue) of TT^{P} in DMSO (n = 16 in all cases).

Table 1. Spectroscopic Properties of TT^{P} Isomers in Solution in DMSO

	(Z)TT^{P}	(E)TT^{P}
λ_{abs} (nm)	357	374
λ_{em} (nm)	480	477
Stokes shift (cm^{-1})	7200	5800
Φ_f	0.025	0.018
σ_{2PA} (GM) [λ_{max} (nm)]	140 [710]	100 [710]

maxima (ca. 710 nm). Consequently, functionalization of this chromophore with the polymeric PHEA chains does not markedly affect its main spectroscopic characteristics as recorded in DMSO solutions.

The fluorescence quantum yields Φ_f of TT^{P} (stereopure (Z) and (E)-forms and (E/Z)-mixture) were also first estimated in DMSO solution, with the aim to highlight the influence of the polymerization degree on this parameter. Indeed, while the quantum yield of the macroinitiator (n = 0 in Figure S17) is ca. Φ_f = 0.004, the addition of polymer chains leads to a moderate yet significant improvement to reach Φ_f = 0.07, a value that subsequently remained constant, within experimental error, for polymer chain lengths between 7 and 70 monomer units

https://doi.org/10.1021/acs.biomac.2c00232
Biomacromolecules 2022, 23, 2485−2495

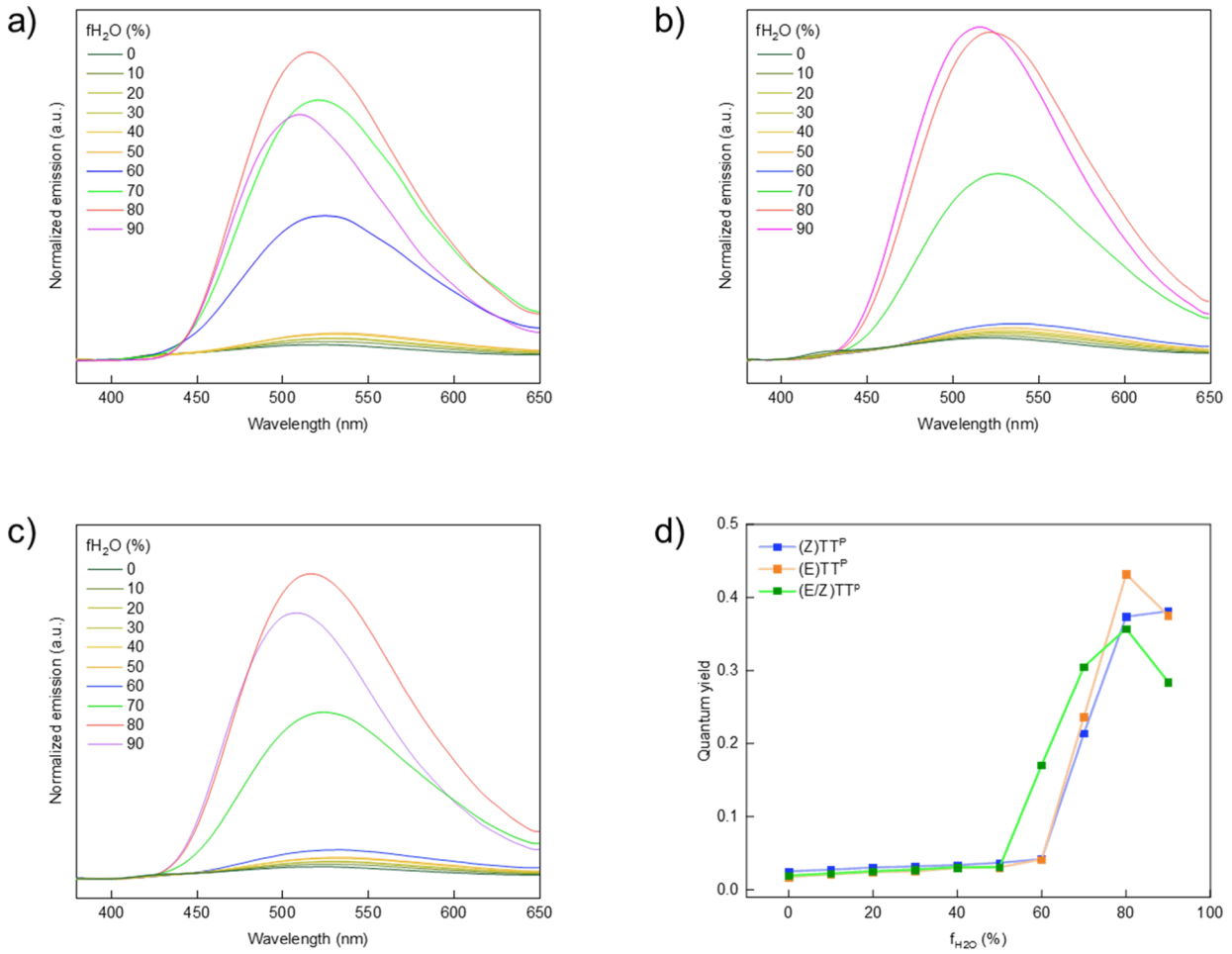

Figure 3. Emission of the (a) isomer mixture, (b) (Z)-isomer, and (c) (E)-isomer of $\mathbf{TT}^{\mathbf{P}}$ (n = 16) in various water/DMSO mixtures. (d) Evolution of the fluorescence quantum efficiency of the isomer mixture (green), (Z)-isomer (blue), and (E)-isomer (orange) of $\mathbf{TT}^{\mathbf{P}}$ in various water/DMSO mixtures.

(Figure S17). Thus, while the introduction of polymer chains seems to favor the emission (probably owing to steric-induced restriction of the rotation around the central double bond, a well-known mechanism in viscosity probes[40]), the effect quickly saturates as the polymer chain is extended, and the emission quantum yield subsequently becomes independent of the length of the PHEA chains. In the rest of this study, we chose to focus on $\mathbf{(E/Z)TT}^{\mathbf{P}}$ with an average polymer chain length n = 16 (as calculated through the comparison of the integration of terminal and main-chain signals, Figure S14), which offers good dispersibility in aqueous media with a limited impact on the molecular weight of the chromophore.

The spectroscopic properties of the PHEA polymers in aqueous media were then studied in DMSO/water mixtures with an increasing water volumic fraction (Figure 3). For a volumic fraction of water f_{H2O} lower than 50%, the emission properties of $\mathbf{(E/Z)TT}^{\mathbf{P}}$ remain virtually constant with $\Phi_f \approx$ 0.07. For f_{H2O} above 50%, a hypsochromic shift from 520 to 467 nm is noticed, consistent with that observed for the parent monomeric fluorophore under similar conditions; this is accompanied by a marked and progressive increase in Φ_f with further addition of water to reach a maximal Φ_f = 0.35 for f_{H2O} of 80% (Figure 3 and Figure S30). These two properties (hypsochromic shift and Φ_f increase) are compatible with the hypothesis of a restriction of the rotation process around the central double bond[41] as a result of interchromophore aggregation in aqueous media. Thus, in contrast with the previously reported similar chromophore polymer adducts,[15−18] the presence of water-solubilizing chains does not suffice to avoid the molecular aggregation of $\mathbf{(E/Z)TT}^{\mathbf{P}}$ at high water contents, and the molecules self-assemble into micellar nanoaggregates.

Similar evolution patterns are observed for the AIE properties of the pure (E) and (Z)-isomers of $\mathbf{TT}^{\mathbf{P}}$, although precipitation onset is shifted to f_{H2O} ca. 60%. At f_{H2O} of 90%, the fluorescence quantum yields of (Z) and (E)-isomers reach maximal Φ_f = 0.38 and 0.37, respectively. These values, similar to those observed with the (E/Z)-mixture of $\mathbf{TT}^{\mathbf{P}}$, are however significantly lower than the values reached in their parent stereopure monomeric analogues in nanosuspensions.[32]

This similarity of AIE properties between the stereopure versions and the mixture of $\mathbf{(E/Z)TT}^{\mathbf{P}}$ thus suggests that the nature of the supramolecular assemblies formed in the case of PHEA chain chromophores does not markedly depend on the stereochemistry of the chromophores. This strikingly differs from our recent observation on similar AIEgens devoid of PHEA side substituents, where the higher crystallinity of the stereopure sample clearly benefited the AIE. In other words, this suggests that, quite expectedly, the presence of the PHEA chain influences the chromophore packing in the nanoassemblies.

https://doi.org/10.1021/acs.biomac.2c00232
Biomacromolecules 2022, 23, 2485−2495

NMR Study of (E/Z)TT^P. To gain understanding on the nature of the interactions between **(E/Z)TT^P** polymers as a function of f_{H2O} and the characteristic size of their assemblies, NMR experiments were then performed in different D_2O/DMSO-d_6 mixtures.

As a first remark, ^{1}H NMR spectra reveal a peculiar evolution of the signal belonging to the chromophoric part and the polymer chains upon increasing f_{D2O} (Figure S15). Indeed, while the signals of the polymer chains remain constant in width and intensity, both the aromatic signals of the chromophore (between 6.80 and 7.45 ppm) and the signal of the two chain-end methyl groups (1.24 ppm) broaden and decrease drastically with an increasing water fraction. At f_{D2O} as low as 10%, these peaks are already hardly distinguishable from the baseline and are no longer visible at f_{D2O} = 50%. It would thus seem that the aggregation phenomena between the hydrophobic parts of the core (chromophore and the attached initiator group) take place in an aqueous medium, in agreement with the spectroscopic evolution observed. Again, this evolution contrasts strongly with previous examples of similar polymer-appended chromophores reported by us,[17] where the relative intensity of the different peaks was unchanged between DMSO-d_6 and D_2O media, characteristic of individual macromolecular objects in solution. Such a behavior is classically observed and has been studied in depth in the past during the self-aggregation process of conjugated polymers such as polythiophenes.[42] It indicates here that, like in the latter, π-stacking unsurprisingly constitutes the main driving force for the self-assembly of the polymer chains.

To investigate this aggregation phenomenon and its dependence on the medium composition and chromophore stereoconfiguration, 2D diffusion-ordered NMR spectroscopy (DOSY) was then used (available as Supporting Information S3, Figures S18−S29).

First, in pure DMSO-d_6 solution, DOSY was used to verify that **(E/Z)TT^P** molecules were present as individual polymer chains and to determine their associated polydispersity index (Đ) with the methodology initially developed by Delsuc et al. and tested in the past on similar polymers.[36,43]

In the case of all samples studied herein, the NMR signals attributed to **(E/Z)TT^P** belong to the same polymer species (with a single diffusion constant; see Figure S18 for a representative case where n = 16). Polydispersity index determination provides a value of Đ = 1.22 for **(E/Z)TT^P** with n = 16 which, although in the high range of what is usually achieved by ATRP, appears satisfactory considering our previous results.[16,17]

In each solvent, the diffusion coefficient value D of a molecule, macromolecule, or nano-object relates to the gyration radius of the latter, considered as a random coil; thus, comparison of the D values obtained for the (Z) and (E)-isomers of **TT^P** featuring similar polymer side-chain lengths (here, n = 16) provides valuable information regarding the impact of stereochemistry on the characteristic dimensions of the associated coil. In DMSO-d_6 solution, similar mean diffusion coefficients are monitored for the (Z) and (E)-isomers (59 and 52 $\mu m^2/s$, respectively), characteristic of a comparable mobility and size for both solvated molecules (Figures S19 and S20). As expected, the average diffusion coefficients D are smaller in D_2O, as a consequence of the aggregation process, yet similar for each isomer (25 for the (E)-isomer and 26 $\mu m^2/s$ for the (Z)-isomer, Figures S21 and S22). This indicates a similar nature for the small-sized nano-objects formed by molecular aggregation in the case of both stereoconfigurations.

In order to get more insights into the aggregation processes taking place at high water contents, we then monitored in a next series of experiments the evolution of the $D_{(E/Z)TT^P}$ coefficients as a function of f_{D2O} (Figure 4 and Table S1).

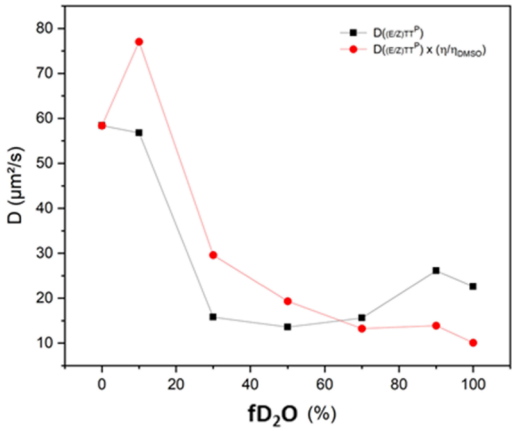

Figure 4. Evolution of the diffusion coefficient of $D_{(E/Z)TT^P}$ (black) and of the viscosity-corrected diffusion coefficient D_η (red) of **(E/Z)TT^P** in DMSO:water mixture with increasing f_{D2O} contents (n = 16 in all cases).

As the spectroscopic studies had already underlined that stereopurity had only little impact on the AIE properties, this study was limited to the (E/Z)-mixture of **TT^P**, available in larger quantities (as typically required for DOSY analyses) than its stereopure analogues. First, a global very noticeable decrease of $D_{(E/Z)TT^P}$ values could be qualitatively observed upon increasing the deuterated water fraction from the initial pure DMSO-d_6 sample, in agreement with the suspected aggregation process (Figures S23−S29). However, when comparing systems in different solvent compositions, the diffusion coefficient of a given object does not solely depend on its radius but also critically on the viscosity of the medium; it is well documented that the latter varies strongly in DMSO/water mixtures depending on the ratio of each solvent.[45] In order to discriminate between both contributions, it is possible and beneficial to use a viscosity-corrected diffusion coefficient. Recent studies have indeed highlighted that, provided that the polymer concentration was kept low in the medium (ca. 1 mg/mL), using such viscosity-corrected values for the diffusion signal allowed a precise evaluation and comparison of macromolecule dimensions even in solvents possessing very different intrinsic viscosities.[44]

We thus considered in a next step the variations of a corrected diffusion coefficient defined for each composition f_{D20} by eq 2:

$$D_\eta = D_{(E/Z)TT^P} \frac{\eta}{\eta_{DMSO}} \quad (2)$$

where η is the viscosity (mPa·s) of the DMSO/water mixture of the considered sample,[45] and η_{DMSO} is the viscosity of pure DMSO.

Using this viscosity-corrected diffusion coefficient, we notice for f_{D20} > 10% a progressive decrease in the corrected diffusion coefficient D_η as f_{D2O} is increased (Figure 4 and Table S1). This confirms that a progressive aggregation process occurs and that the average size of the resulting nanoaggregates gets

https://doi.org/10.1021/acs.biomac.2c00232
Biomacromolecules 2022, 23, 2485−2495

bigger and eventually reaches a maximal size in pure water, in agreement with the observed AIE evolution.

The Stokes–Einstein equation relates the diffusion coefficient D of a well-defined spherical nano-object to its radius r, according to eq 3:

$$D = \frac{k_b T}{6\pi\eta r} \tag{3}$$

where k_b is the Boltzmann constant (1.380649×10^{-23} J K^{-1}), T is the temperature in Kelvin (here taken as 298 K), and η is the dynamic viscosity, in Pa·s. The latter is well known and has been tabulated in the past for different DMSO/water mixtures.[45]

Using these tabulated values, we calculated a nanoparticle radius (considered as rigid spheres) ca. 7 nm in DMSO-d_6:D_2O, 70:30 (v/v, corresponding to the onset of the self-assembly process). In pure water, it culminates to about 9 nm, that is, a diameter of about 18 nm, in the spherical assumption.

DLS and TEM Studies. Although DOSY NMR brings conclusive evidence for the formation of nanoparticles by the self-assembly of **(E/Z)TT^P** at a high water content, extrapolation of the characteristic size of the nano-object's diffusion coefficient is inherently prone to error, specifically for nonrigid and nonperfectly spherical nano-objects.[46,47] In order to get additional and complementary insights on the dimensions of the self-assembled nanoparticles, DLS experiments were thus undertaken on the aqueous suspensions of **(E/Z)TT^P** (n = 16). As expected, no scattering signal was obtained for the initial solution of the (E/Z)-mixture of **TT^P** in DMSO. Similarly, no reliable DLS correlogram could be obtained for both isomers (Figure 5), with f_{H2O} < 70%. Again,

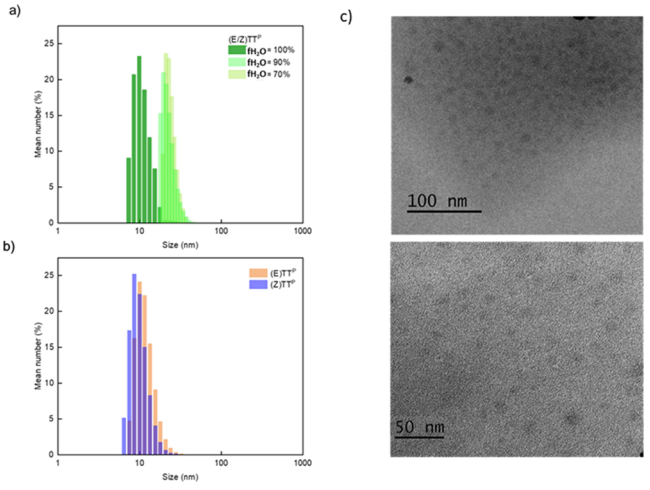

Figure 5. DLS of (a) (E/Z)-mixture of **TT^P** in DMSO/water mixture and (b) stereopure **TT^P** in water. (c) Low-resolution TEM pictures of **(E/Z)TT^P** nanoparticles on a TEM grid, with two different magnifications.

in contrast with what had been noticed in our previous work with the monomeric analogues **(E/Z)TT^{OMe}**, where nanoprecipitation in water resulted in the formation of particles with an average diameter of 150–200 nm,[32] an homogeneous suspension of small nanoparticles was observed here: for f_{H2O} = 70%, d = 25 nm (PDI = 0.29) and for f_{H2O} = 90%, d = 26 nm (PDI = 0.28; Figure 5). Then, upon simple mixing of the dry polymeric materials in pure distilled water, this average size is halved (around 10 nm for **(E/Z)TT^P**; PDI = 0.42), and slightly larger nanosuspensions are observed for the (E)-isomer compared to (Z) (12 vs 10 nm, PDI = 0.46 vs PDI = 0.42, Figures 5 and S31–S32). As expected, this result indicates that the bola-amphiphilic nature of our polymer-appended chromophore favors the controlled formation of small and monodisperse nano-objects, ideally suited for biorelated applications. This was further verified by performing low-resolution TEM measurements on **(E/Z)TT^P**. Although the obtained images present only limited contrast because of the pure organic nature of the studied compound, they confirm the formation of spherical organic nanoparticles with an average diameter of ca. 10–15 nm, in good agreement with what had been calculated through both DOSY and DLS measurements (Figures 5c and S34–S36).

Determination of the Critical Micellar Concentration. Last, the critical micellar concentration (CMC) was determined using SFT measurements on the stereoisomer mixture **(E/Z)TT^P**. Plotting the evolution of the surface tension versus logarithm of the concentration of **(E/Z)TT^P** (Figures 6 and S33) yields two distinct evolution:

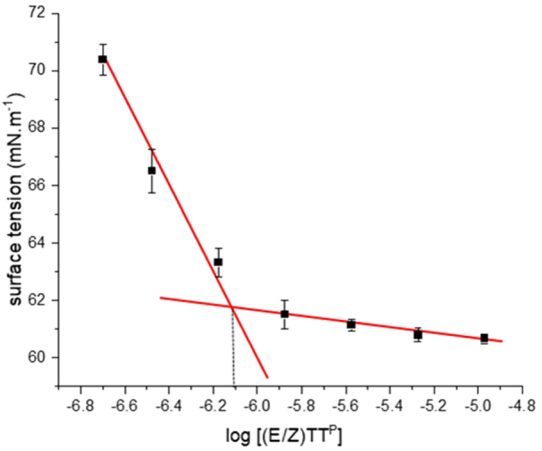

Figure 6. Plot of the evolution of the measured surface tension vs logarithm of the concentration of **(E/Z)TT^P** in water (25 °C). Intercept of the two linear trends provides access to the CMC value.

above the CMC, only little variations of surface tension are observed when varying the polymer concentration, and a quasi-plateau is obtained with a surface tension of about 61 mN·m^{-1}. Below the CMC, surface tension decreases steadily upon increasing the concentration of **(E/Z)TT^P**. The CMC (onset concentration of micelle formation) can be determined by checking the intercept of these two linear trends (in linear/log scales), which is found here as ca. 0.75 μM, a value much below the concentrations used in the abovementioned studies and relevant for biological investigations.

Biological Studies. In a previous report, we showed that suspensions of nonpolymeric **(E/Z)TT^{OMe}** were efficient in providing highly contrasted two-photon fluorescence microscopy images, both in cellulo and in vivo (after injection in the caudal vein of zebrafish embryos). However, long-term following of the fate of the zebrafish embryos revealed that various malformations and premature death occurred within days after injections, raising important issues regarding the biocompatibility of these nano-objects. Size and surface functionalization of nanoparticles are indeed two important parameters that largely determine their fate and biocompati-

https://doi.org/10.1021/acs.biomac.2c00232
Biomacromolecules 2022, 23, 2485–2495

bility in living systems, both of which turned out to be suboptimal in this initial work.

As our present study allowed us to underline several promising features of (E/Z)TT^{P} as potential two-photon luminescent contrast agents, we decided to further investigate this point using similar setups and biological systems as in our abovementioned work. More specifically, we aimed at establishing whether the adjunction of polymer side substituents and the resulting impact on the features of the self-assembled nanosystems could be beneficial in terms of biocompatibility.

In a first step, we studied the biocompatibility of such compounds on human cells in culture. The goal was to determine the maximal concentration that could be used while avoiding any significant cell death. To that end, the increasing concentrations of compounds in the isomeric (Z) and (E)-forms were incubated with MCF-7 cells for 3 days. The result reported in Figure 7a suggested that, even at high concentrations such as 150 μg mL^{-1}, both compounds were safe for the cell. In Figure 7b, we can see that both compounds are highly luminescent (green dots) and efficiently internalized in the cancer cells, the plasmatic membranes of which are stained with CellMask (in red). In this experiment, isomers in living cells were revealed by two-photon excitation at 750 nm excitation wavelength. This imaging potential seems very similar to those obtained in our previous report on (E/Z)TT^{OMe}.

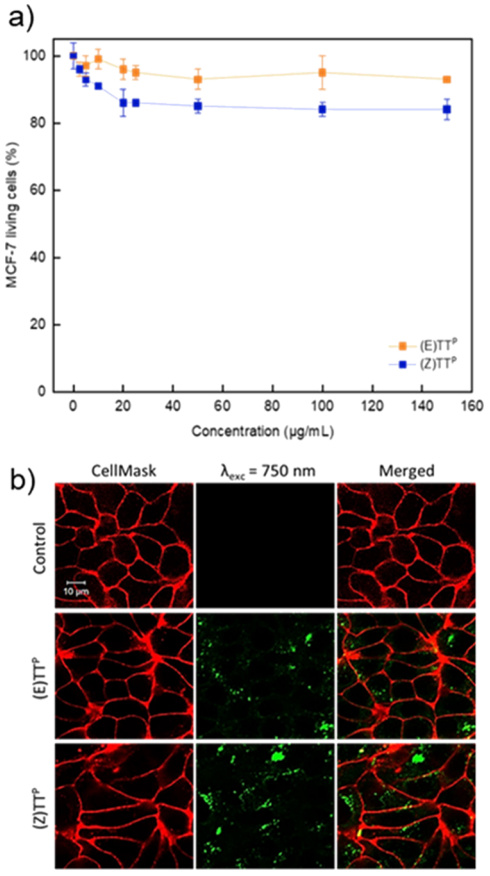

Figure 7. In cellulo studies. (a) Cytotoxic study of (E) and (Z)-isomers of TT^{P} (n = 16). Increasing concentrations (from 2.5 to 150 μg mL^{-1}) of compounds were incubated with MCF-7 cells for 3 days, and the percentage of living cells was quantified by MTT assay. (b) Confocal microscopy imaging of living MCF-7 cells after 24 h incubation with 50 μg mL^{-1} of (E) or (Z)-isomers (green dots). Isomers were revealed by two-photon excitation at λ_{exc} = 750 nm (Chameleon, LSM 780), and cell membranes (red outlines) were stained with CellMask Orange ($\lambda_{exc}/\lambda_{em}$ = 554/567 nm). Scale bars = 10 μm.

Then, to determine the possibility for biomedical use, the imaging potential was analyzed in vivo in zebrafish embryos. After injection in the caudal vein, TT^{P}, either in its (E) or (Z)-forms, provides a high luminescence signal visible under UV light excitation (pseudocolor green, Figure 8a) and exhibits high solubility and bioavailability in all organisms. Importantly, the luminescence of these compounds was also investigated in two-photon microscopy conditions under pulsed laser excitation (Figure 8b). A strong capability of imaging was observed when excited at 750 nm, similar to that achieved in our aforementioned report.[32]

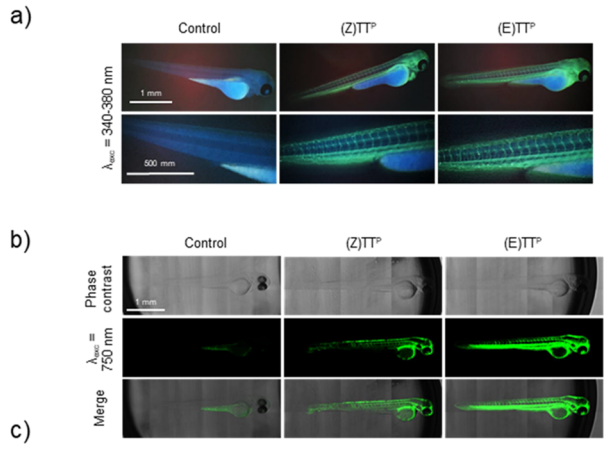

Toxicity study	Control (n = 7)	(Z)TT^{P} (n = 9)	(E)TT^{P} (n = 10)
Movements	+++	+++	+++
Stable heart rate	+++	+++	+++
Malformations	---	---	---
Deaths	---	---	---

Figure 8. In vivo studies. Casper zebrafish embryos of 72 hpf were intravenously injected with 10 nL of TT^{P} ((Z) or (E)-isomers in their pure form, n = 16) at 1 mg mL^{-1}. One hour after injection, embryos were observed using (a) one-photon excitation microscopy at 340−380 nm and (b) two-photon excitation microscopy at 750 nm. (c) Embryos were then maintained 3 days under breeding conditions to analyze everyday the biocompatibility of (Z) or (E)-isomers, according to the parameters reported in the table, with "+" for presence and "−" for absence.

In parallel, the biocompatibility of both isomers injected in the bloodstream of embryos was studied. For 3 days, the embryos' development, heart rate, and mobility were monitored daily. The data reported in the table (Figure 8c) demonstrate that for both isomers no toxicity could be detected in zebrafish embryos in the studied conditions, translating into no increase in the mortality of the said embryos. Survival and development of the zebrafish embryos, as monitored over several days, are indeed perfectly similar in the treated and control embryos. These results constitute a marked improvement in comparison with our recently published results with nanoprecipitated assemblies of TT^{OMe} chromophores and highlight the strong potential of TT^{P} for long-term bioimaging of living organisms.

https://doi.org/10.1021/acs.biomac.2c00232
Biomacromolecules 2022, 23, 2485−2495

CONCLUSIONS

In this paper, we illustrate the benefits in functionalizing TPE-based AIEgens, the structures of which are specifically optimized for two-photon-induced emission properties at the solid state, with hydrophilic polymer side chains. In DMSO, the resulting bola-amphiphilic macromolecular chromophores **(E/Z)TT^P** exist as individual, low-emissive ($\Phi_f \approx 0.07$) polymer chains. This is attested by DOSY NMR experiments, which indicate that, for both the (Z) and (E)-isomers, a similar length of polymer arms (n = 16 units) and a similar low polydispersity ($Đ$ = 1.22) can be achieved, in agreement with the controlled nature of the radical polymerization.

In contrast, when dispersed in water, either from nanoprecipitation of a concentrated solution of the molecule in DMSO or by direct mixing of the polymer powder in pure water or physiological solution, a characteristic AIE phenomenon is observed which correlates to the formation of small nanobundles of several chromophore units of **(E/Z)TT^P**. DLS analyses carried out on both the (Z) and (E)-isomers validate the presence of nanoaggregates at $f_{H2O} > 0.5$, with a mean size of ca. 10−15 nm and a low dispersity, which is further confirmed by TEM imaging. To refine our understanding of the aggregation process dynamics, DOSY experiments over the whole range of f_{H2O} gave additional insights on the formation of these aggregates. The latter is characterized by a progressive restriction in the measured diffusion coefficient for chemical shifts belonging to the polymer chain upon increasing f_{H2O}, to reach its lowest value in pure water, confirming that a self-assembly process drives the formation of the fluorescent organic nanoparticles. In pure water, CMC of **(E/Z)TT^P** is about 0.75 μM. It is thereby confirmed that the strategy introduced herein is efficient in yielding ultra-bright, two-photon active organic nanoparticles with features optimized with regard to the target biological applications.

To illustrate the benefits of our approach in the specific framework of intravital bioimaging, the resulting aqueous suspensions of both (Z) and (E) stereopure **TT^P** (f_{H2O} = 100%) were used as nanosized fluorescent organic nanoparticle contrast agents in epifluorescence and two-photon fluorescence microscopy of the vascular systems of zebrafish embryos. Besides the favorable spectroscopic properties of the nano-objects, which afforded in all cases highly contrasted images, a distinctive advantage of the polymer-functionalized two-photon AIEgens reported herein in comparison with their molecular analogues is their much improved biocompatibility, which enables long-term studies on living systems and might constitute a keystone and determining feature of this strategy toward its possible future use in biomedical contexts.

ASSOCIATED CONTENT

Supporting Information

The Supporting Information is available free of charge at https://pubs.acs.org/doi/10.1021/acs.biomac.2c00232.

Detailed synthetic procedures; hard copies of ^{1}H and ^{13}C NMR spectra for all new molecules and polymers; conditions for the separation of chromophoric macro-initiators by preparative HPLC on chiral stationary phases and associated chromatograms; complementary fluorescence studies regarding the dependence on fluorescence quantum yield to polymer length; hard copies of all DOSY NMR spectra used in the study; pictures of 2 × 10^{-5} M **(E/Z)TT^P** in different DMSO/H_2O mixtures (f_{H2O} from 0 to 100%); surface tension measurements data; and additional TEM images (PDF)

AUTHOR INFORMATION

Corresponding Authors

Magali Gary-Bobo − *IBMM, Univ. Montpellier, CNRS, ENSCM, Montpellier 34293, France*; Email: magali.gary-bobo@inserm.fr

Cyrille Monnereau − *Univ. Lyon, ENS Lyon, CNRS, Laboratoire de Chimie, UMR 5182, 69364 Lyon, France*; orcid.org/0000-0002-8928-2416; Email: cyrille.monnereau@ens-lyon.fr

Authors

Jean Rouillon − *Univ. Lyon, ENS Lyon, CNRS, Laboratoire de Chimie, UMR 5182, 69364 Lyon, France*; Present Address: Department of Chemistry and Chemical Engineering, Chalmers University of Technology, Göteborg 412 96, Sweden; orcid.org/0000-0001-7823-7575

Lamiaa M. A. Ali − *IBMM, Univ. Montpellier, CNRS, ENSCM, Montpellier 34293, France; Department of Biochemistry Medical Research Institute, University of Alexandria, 21561 Alexandria, Egypt*; orcid.org/0000-0003-1176-5335

Kamel Hadj-Kaddour − *IBMM, Univ. Montpellier, CNRS, ENSCM, Montpellier 34293, France*

Raphaël Marie-Luce − *Univ. Lyon, ENS Lyon, CNRS, Laboratoire de Chimie, UMR 5182, 69364 Lyon, France*

Guillaume Simon − *Univ. Lyon, ENS Lyon, CNRS, Laboratoire de Chimie, UMR 5182, 69364 Lyon, France*; orcid.org/0000-0003-0154-0765

Mélanie Onofre − *IBMM, Univ. Montpellier, CNRS, ENSCM, Montpellier 34293, France*

Sandrine Denis-Quanquin − *Univ. Lyon, ENS Lyon, CNRS, Laboratoire de Chimie, UMR 5182, 69364 Lyon, France*

Marion Jean − *Aix Marseille University, CNRS, Centrale Marseille, iSm2, Marseille 13284, France*; orcid.org/0000-0003-0524-8825

Muriel Albalat − *Aix Marseille University, CNRS, Centrale Marseille, iSm2, Marseille 13284, France*

Nicolas Vanthuyne − *Aix Marseille University, CNRS, Centrale Marseille, iSm2, Marseille 13284, France*; orcid.org/0000-0003-2598-7940

Guillaume Micouin − *Univ. Lyon, ENS Lyon, CNRS, Laboratoire de Chimie, UMR 5182, 69364 Lyon, France*

Akos Banyasz − *Univ. Lyon, ENS Lyon, CNRS, Laboratoire de Chimie, UMR 5182, 69364 Lyon, France*

Chantal Andraud − *Univ. Lyon, ENS Lyon, CNRS, Laboratoire de Chimie, UMR 5182, 69364 Lyon, France*

Complete contact information is available at: https://pubs.acs.org/10.1021/acs.biomac.2c00232

Author Contributions

The manuscript was written through contributions of all authors. All authors have given approval to the final version of the manuscript.

Funding

The imaging facility MRI is a member of the national infrastructure France-BioImaging supported by the French National Research Agency (ANR-10-INBS-04, ≪Investments for the future≫).

Notes

The authors declare no competing financial interest.

■ ACKNOWLEDGMENTS

All authors would like to thank Mireille Rossel and Nicolas Cubedo for their technical assistance in zebrafish experiments. In addition, the authors acknowledge the imaging facility MRI for allowing access to the imaging platform. The authors thank Margarida F. Costa-Gomes for kindly granting full access to the viscosimeter. The authors thank the Centre Technologique des Microstructures (CTμ) at the Université Claude Bernard Lyon 1 and especially Xavier Jaurand for granting access to the microscopy platform and kind assistance in the TEM measurements.

■ ABBREVIATIONS

ATRP, atom transfer radical polymerization; $CDCl_3$, deuterated chloroform; DLS, dynamic light scattering; DMSO-d_6, deuterated dimethylsulfoxide; DOSY, diffusion ordered spectroscopy; f_{H2O}, f_{D2O}, volume fraction of water and deuterated water, respectively; LSM, laser scanning microscopy; NMR, nuclear magnetic resonance; TBAF, tetrabutylammonium fluoride; TPEF, two-photon excited fluorescence.

■ REFERENCES

(1) Helmchen, F.; Denk, W. Deep tissue two-photon microscopy. *Nat. Methods* **2005**, *2*, 932−940.
(2) So, P. T. C.; Dong, C. Y.; Masters, B. R.; Berland, K. M. Two-Photon Excitation Fluorescence Microscopy. *Annu. Rev. Biomed. Eng.* **2000**, *2*, 399−429.
(3) Ellis-Davies, G. C. R. Two-Photon Microscopy for Chemical Neuroscience. *ACS Chem. Neurosci.* **2011**, *2*, 185−197.
(4) Shih, A. Y.; Driscoll, J. D.; Drew, P. J.; Nishimura, N.; Schaffer, C. B.; Kleinfeld, D. Two-Photon Microscopy as a Tool to Study Blood Flow and Neurovascular Coupling in the Rodent Brain. *J. Cereb. Blood Flow Metab.* **2012**, *32*, 1277−1309.
(5) McDole, K.; Xiong, Y.; Iglesias, P. A.; Zheng, Y. Lineage mapping the pre-implantation mouse embryo by two-photon microscopy, new insights into the segregation of cell fates. *Dev. Biol.* **2011**, *355*, 239−249.
(6) Schenke-Layland, K.; Riemann, I.; Damour, O.; Stock, U. A.; König, K. Two-photon microscopes and in vivo multiphoton tomographs — Powerful diagnostic tools for tissue engineering and drug delivery. *Adv. Drug Delivery Rev.* **2006**, *58*, 878−896.
(7) Ibraheem, A.; Campbell, R. E. Designs and applications of fluorescent protein-based biosensors. *Curr. Opin. Chem. Biol.* **2010**, *14*, 30−36.
(8) Miller, D. R.; Jarrett, J. W.; Hassan, A. M.; Dunn, A. K. Deep tissue imaging with multiphoton fluorescence microscopy. *Curr. Opin. Biomed. Eng.* **2017**, *4*, 32−39.
(9) Drobizhev, M.; Makarov, N. S.; Tillo, S. E.; Hughes, T. E.; Rebane, A. Two-photon absorption properties of fluorescent proteins. *Nat. Methods* **2011**, *8*, 393−399.
(10) Yao, S.; Belfield, K. D. Two-Photon Fluorescent Probes for Bioimaging. *Eur. J. Org. Chem.* **2012**, *2012*, 3199−3217.
(11) Lou, X.; Zhao, Z.; Tang, B. Z. Organic Dots Based on AIEgens for Two-Photon Fluorescence Bioimaging. *Small* **2016**, *12*, 6430−6450.
(12) Adjili, S.; Favier, A.; Fargier, G.; Thomas, A.; Massin, J.; Monier, K.; Favard, C.; Vanbelle, C.; Bruneau, S.; Peyriéras, N.; Andraud, C.; Muriaux, D.; Charreyre, M.-T. Biocompatible photoresistant far-red emitting, fluorescent polymer probes, with near-infrared two-photon absorption, for living cell and zebrafish embryo imaging. *Biomaterials* **2015**, *46*, 70−81.
(13) Bui, A. T.; Beyler, M.; Grichine, A.; Duperray, A.; Mulatier, J.-C.; Guyot, Y.; Andraud, C.; Tripier, R.; Brasselet, S.; Maury, O. Near infrared two photon imaging using a bright cationic Yb(iii) bioprobe spontaneously internalized into live cells. *Chem. Commun.* **2017**, *53*, 6005−6008.
(14) Navarro, J. R. G.; Lerouge, F.; Cepraga, C.; Micouin, G.; Favier, A.; Chateau, D.; Charreyre, M.-T.; Lanoë, P.-H.; Monnereau, C.; Chaput, F.; Marotte, S.; Leverrier, Y.; Marvel, J.; Kamada, K.; Andraud, C.; Baldeck, P. L.; Parola, S. Nanocarriers with ultrahigh chromophore loading for fluorescence bio-imaging and photodynamic therapy. *Biomaterials* **2013**, *34*, 8344−8351.
(15) Monnereau, C.; Marotte, S.; Lanoë, P.-H.; Maury, O.; Baldeck, P. L.; Kreher, D.; Favier, A.; Charreyre, M.-T.; Marvel, J.; Leverrier, Y.; Andraud, C. Water-soluble chromophores with star-shaped oligomeric arms: synthesis, spectroscopic studies and first results in bio-imaging and cell death induction. *New J. Chem.* **2012**, *36*, 2328−2333.
(16) Massin, J.; Charaf-Eddin, A.; Appaix, F.; Bretonnière, Y.; Jacquemin, D.; van der Sanden, B.; Monnereau, C.; Andraud, C. A water soluble probe with near infrared two-photon absorption and polarity-induced fluorescence for cerebral vascular imaging. *Chem. Sci.* **2013**, *4*, 2833−2843.
(17) Pascal, S.; Denis-Quanquin, S.; Appaix, F.; Duperray, A.; Grichine, A.; Le Guennic, B.; Jacquemin, D.; Cuny, J.; Chi, S.-H.; Perry, J. W.; van der Sanden, B.; Monnereau, C.; Andraud, C.; Maury, O. Keto-polymethines: a versatile class of dyes with outstanding spectroscopic properties for in cellulo and in vivo two-photon microscopy imaging. *Chem. Sci.* **2017**, *8*, 381−394.
(18) Mettra, B.; Appaix, F.; Olesiak-Banska, J.; Le Bahers, T.; Leung, A.; Matczyszyn, K.; Samoc, M.; van der Sanden, B.; Monnereau, C.; Andraud, C. A Fluorescent Polymer Probe with High Selectivity toward Vascular Endothelial Cells for and beyond Noninvasive Two-Photon Intravital Imaging of Brain Vasculature. *ACS Appl. Mater. Interfaces* **2016**, *8*, 17047−17059.
(19) Deiana, M.; Mettra, B.; Matczyszyn, K.; Piela, K.; Pitrat, D.; Olesiak-Banska, J.; Monnereau, C.; Andraud, C.; Samoc, M. Interactions of a biocompatible water-soluble anthracenyl polymer derivative with double-stranded DNA. *Phys. Chem. Chem. Phys.* **2015**, *17*, 30318−30327.
(20) Deiana, M.; Mettra, B.; Martinez-Fernandez, L.; Mazur, L. M.; Pawlik, K.; Andraud, C.; Samoc, M.; Improta, R.; Monnereau, C.; Matczyszyn, K. Specific Recognition of G-Quadruplexes Over Duplex-DNA by a Macromolecular NIR Two-Photon Fluorescent Probe. *J. Phys. Chem. Lett.* **2017**, *8*, 5915−5920.
(21) Deiana, M.; Mettra, B.; Matczyszyn, K.; Pitrat, D.; Olesiak-Banska, J.; Monnereau, C.; Andraud, C.; Samoc, M. Unravelling the Binding Mechanism of a Poly(cationic) Anthracenyl Fluorescent Probe with High Affinity toward Double-Stranded DNA. *Biomacromolecules* **2016**, *17*, 3609−3618.
(22) Deiana, M.; Mettra, B.; Mazur, L. M.; Andraud, C.; Samoc, M.; Monnereau, C.; Matczyszyn, K. Two-Photon Macromolecular Probe Based on a Quadrupolar Anthracenyl Scaffold for Sensitive Recognition of Serum Proteins under Simulated Physiological Conditions. *ACS Omega* **2017**, *2*, 5715−5725.
(23) Yang, Z.; Chi, Z.; Mao, Z.; Zhang, Y.; Liu, S.; Zhao, J.; Aldred, M. P.; Chi, Z. Recent advances in mechano-responsive luminescence of tetraphenylethylene derivatives with aggregation-induced emission properties. *Mater. Chem. Front.* **2018**, *2*, 861−890.
(24) Leung, N. L. C.; Xie, N.; Yuan, W.; Liu, Y.; Wu, Q.; Peng, Q.; Miao, Q.; Lam, J. W. Y.; Tang, B. Z. Restriction of Intramolecular Motions: The General Mechanism behind Aggregation-Induced Emission. *Chem. − Eur. J.* **2014**, *20*, 15349−15353.
(25) Zhao, Z.; Zhang, H.; Lam, J. W. Y.; Tang, B. Z. Aggregation-Induced Emission: New Vistas at the Aggregate Level. *Angew. Chem., Int. Ed.* **2020**, *59*, 9888−9907.
(26) Lin, J.; Zeng, X.; Xiao, Y.; Tang, L.; Nong, J.; Liu, Y.; Zhou, H.; Ding, B.; Xu, F.; Tong, H.; Deng, Z.; Hong, X. Novel near-infrared II aggregation-induced emission dots for in vivo bioimaging. *Chem. Sci.* **2019**, *10*, 1219−1226.
(27) Tong, H.; Hong, Y.; Dong, Y.; Häußler, M.; Lam, J. W. Y.; Li, Z.; Guo, Z.; Guo, Z.; Tang, B. Z. Fluorescent "light-up" bioprobes

https://doi.org/10.1021/acs.biomac.2c00232
Biomacromolecules 2022, 23, 2485−2495

based on tetraphenylethylene derivatives with aggregation-induced emission characteristics. *Chem. Commun.* **2006**, *35*, 3705−3707.
(28) Zhu, X.; Wang, J.-X.; Niu, L.-Y.; Yang, Q.-Z. Aggregation-Induced Emission Materials with Narrowed Emission Band by Light-Harvesting Strategy: Fluorescence and Chemiluminescence Imaging. *Chem. Mater.* **2019**, *31*, 3573−3581.
(29) Wang, Z.; Yong, T.-Y.; Wan, J.; Li, Z.-H.; Zhao, H.; Zhao, Y.; Gan, L.; Yang, X.-L.; Xu, H.-B.; Zhang, C. Temperature-Sensitive Fluorescent Organic Nanoparticles with Aggregation-Induced Emission for Long-Term Cellular Tracing. *ACS Appl. Mater. Interfaces* **2015**, *7*, 3420−3425.
(30) Li, B.; Chen, T.; Wang, Z.; Guo, Z.; Peña, J.; Zeng, L.; Xing, J. A novel cross-linked nanoparticle with aggregation-induced emission properties for cancer cell imaging. *J. Mater. Chem. B* **2020**, *8*, 2431−2437.
(31) Zhang, N.; Chen, H.; Fan, Y.; Zhou, L.; Trépout, S.; Guo, J.; Li, M.-H. Fluorescent Polymersomes with Aggregation-Induced Emission. *ACS Nano* **2018**, *12*, 4025−4035.
(32) Rouillon, J.; Blahut, J.; Jean, M.; Albalat, M.; Vanthuyne, N.; Lesage, A.; Ali, L. M. A.; Hadj-Kaddour, K.; Onofre, M.; Gary-Bobo, M.; Micouin, G.; Banyasz, A.; Le Bahers, T.; Andraud, C.; Monnereau, C. Two-Photon Absorbing AIEgens: Influence of Stereoconfiguration on Their Crystallinity and Spectroscopic Properties and Applications in Bioimaging. *ACS Appl. Mater. Interfaces* **2020**, *12*, 55157−55168.
(33) Reisch, A.; Klymchenko, A. S. Fluorescent Polymer Nanoparticles Based on Dyes: Seeking Brighter Tools for Bioimaging. *Small* **2016**, *12*, 1968−1992.
(34) Collot, M.; Schild, J.; Fam, K. T.; Bouchaala, R.; Klymchenko, A. S. Stealth and Bright Monomolecular Fluorescent Organic Nanoparticles Based on Folded Amphiphilic Polymer. *ACS Nano* **2020**, *14*, 13924−13937.
(35) Gamucci, O.; Bertero, A.; Gagliardi, M.; Bardi, G. Biomedical Nanoparticles: Overview of Their Surface Immune-Compatibility. *Coatings* **2014**, *4*, 139−159.
(36) Viéville, J.; Tanty, M.; Delsuc, M.-A. Polydispersity index of polymers revealed by DOSY NMR. *J. Magn. Reson.* **2011**, *212*, 169−173.
(37) Berry, J. D.; Neeson, M. J.; Dagastine, R. R.; Chan, D. Y. C.; Tabor, R. F. Measurement of surface and interfacial tension using pendant drop tensiometry. *J. Colloid Interface Sci.* **2015**, *454*, 226−237.
(38) de Reguardati, S.; Pahapill, J.; Mikhailov, A.; Stepanenko, Y.; Rebane, A. High-accuracy reference standards for two-photon absorption in the 680-1050 nm wavelength range. *Opt. Express* **2016**, *24*, 9053−9066.
(39) Harris, M. C.; Huang, X.; Buchwald, S. L. Improved Functional Group Compatibility in the Palladium-Catalyzed Synthesis of Aryl Amines. *Org. Lett.* **2002**, *4*, 2885−2888.
(40) Ma, C.; Sun, W.; Xu, L.; Qian, Y.; Dai, J.; Zhong, G.; Hou, Y.; Liu, J.; Shen, B. A minireview of viscosity-sensitive fluorescent probes: design and biological applications. *J. Mater. Chem. B* **2020**, *8*, 9642−9651.
(41) Rouillon, J.; Monnereau, C.; Andraud, C. Reevaluating the Solution Photophysics of Tetraphenylethylene at the Origin of their Aggregation-Induced Emission Properties. *Chem. − Eur. J.* **2021**, *27*, 8003−8007.
(42) Parenti, F.; Tassinari, F.; Libertini, E.; Lanzi, M.; Mucci, A. Π-Stacking Signature in NMR Solution Spectra of Thiophene-Based Conjugated Polymers. *ACS Omega* **2017**, *2*, 5775−5784.
(43) Appukuttan, V. K.; Dupont, A.; Denis-Quanquin, S.; Andraud, C.; Monnereau, C. Mild and efficient bromination of poly-(hydroxyethyl acrylate) and its use towards ionic-liquid containing polymers. *Polym. Chem.* **2012**, *3*, 2723−2726.
(44) Nieto-Draghi, C.; Ávalos, J. B.; Rousseau, B. Transport properties of dimethyl sulfoxide aqueous solutions. *J. Chem. Phys.* **2003**, *119*, 4782−4789.
(45) LeBel, R. G.; Goring, D. A. I. Density, Viscosity, Refractive Index, and Hygroscopicity of Mixtures of Water and Dimethyl Sulfoxide. *J. Chem. Eng. Data* **1962**, *7*, 100−101.
(46) Hinton, D. P.; Johnson, C. S. Diffusion ordered 2D NMR spectroscopy of phospholipid vesicles: determination of vesicle size distributions. *J. Phys. Chem.* **1993**, *97*, 9064−9072.
(47) Canzi, G.; Mrse, A. A.; Kubiak, C. P. Diffusion-Ordered NMR Spectroscopy as a Reliable Alternative to TEM for Determining the Size of Gold Nanoparticles in Organic Solutions. *J. Phys. Chem. C* **2011**, *115*, 7972−7978.

https://doi.org/10.1021/acs.biomac.2c00232
Biomacromolecules 2022, 23, 2485−2495